Research Square

Preprints are preliminary reports that have not undergone peer review.
They should not be considered conclusive, used to inform clinical practice,
or referenced by the media as validated information.

Connectivity-dependent effects of depth-1 canalisation on attractor dynamics in small-world Boolean networks

Maram Alqarni

maram.alqarni@student.uq.edu.au

The University of Queensland

Mark Cooper

The University of Queensland

Diane Donovan

The University of Queensland

James Lefevre

The University of Queensland

Article

Keywords: Boolean networks, canalisation, small-world networks, attractors, perturbation recovery, gene regulatory networks

Posted Date: November 3rd, 2026

DOI: https://doi.org/10.21203/rs.3.rs-11317344/v1

License: This work is licensed under a Creative Commons Attribution 4.0 International License.
Read Full License

Additional Declarations: No competing interests reported.

Connectivity-dependent effects of depth-1 canalisation on attractor dynamics in small-world Boolean networks

Maram Alqarni[1,2,3,*], Mark Cooper[3,4,5], Diane Donovan[2,3], and James Lefevre[2,3]

[1]Department of Mathematics, College of Science, University of Bisha, Bisha, Saudi Arabia
[2]School of Mathematics and Physics, The University of Queensland, Brisbane, 4072, Australia
[3]ARC Centre of Excellence for Plant Success in Nature and Agriculture, The University of Queensland, Brisbane, Queensland, Australia
[4]Queensland Alliance for Agriculture and Food Innovation (QAAFI), Centre for Crop Science, The University of Queensland, Saint Lucia, Queensland, Australia
[5]ARC Training Centre in Predictive Breeding, The University of Queensland, Saint Lucia, Queensland, Australia
[*]Corresponding author: Maram Alqarni. School of Mathematics and Physics, The University of Queensland, Brisbane 4072, Australia. Email: maram.alqarni@student.uq.edu.au

Abstract

Boolean networks provide a framework for studying how network structure and local rules shape long-term dynamics. We studied synchronously updated, directed, signed Watts–Strogatz Boolean networks with depth-1 canalising threshold rules, using 825,000 graph–rule replicates across five controlled parameters. Connectivity reversed the adjusted period effect of full canalisation relative to threshold-only rules. At network size $N = 100$, full canalisation increased the adjusted geometric mean period by 22.1–25.8% at neighbourhood parameter $\kappa = 1$, but shortened it at $\kappa = 2$–5 across all five inhibitory-edge probabilities, with contrasts averaged equally over simulated rewiring probabilities. The magnitude depended on inhibitory-edge probability and rewiring. Increasing rewiring from $p = 0.01$ to $p = 0.60$ shortened adjusted periods after averaging over other simulated settings. Full canalisation lowered, rather than increased, the fixed-point rate. A separate design of 7,200 fixed Boolean systems at inhibitory-edge probabilities 0.30 and 0.50 examined sampled basins and one-bit perturbations. Full canalisation reduced the number of attractors reached from sampled initial states, increased return probability within 2000 updates, and reduced restricted mean return time and mean Hamming fraction after 25 updates. These findings identify a connectivity-dependent period response within the tested model and sampling design.

Keywords: Boolean networks; canalisation; small-world networks; attractors; perturbation recovery; gene regulatory networks.

1 Introduction

Gene regulatory networks control how genes are turned on and off, and how cells respond to internal and external signals. When modelling biological systems, the detailed rate parameters needed for continuous models are not always available. Some regulatory interactions may still be known, allowing the network structure to be represented as a graph. Discrete Boolean networks provide an alternative because they represent each component as a binary state and describe regulation through logical update rules [1, 2, 3, 4]. Thus Boolean networks (BNs) provide a compact lan-

guage for studying how the wiring of a regulatory system shapes its long-term behaviour [1, 5, 6]. Each node holds a binary state (on/off); at discrete time steps all nodes update according to local logical rules that encode activation and repression by neighbouring nodes, and all nonzero edge weights remain fixed at ± 1.

In a biological setting, attractors are often interpreted as coarse descriptions of stable cell states, phenotypes, or recurring regulatory programmes, while basins describe the initial states that lead to those long-term behaviours [3, 4, 7]. In a deterministic Boolean network, each trajectory in the finite state space must eventually repeat, forming what is known as an attractor. The period L of an attractor is a useful summary of network dynamics and allows comparisons across different network structures and rule settings [3, 8, 9].

Attractor period alone does not describe the whole sampled long-term behaviour. Two Boolean systems may have similar periods but differ in the number of attractors reached from sampled initial states, the distribution of sampled basin sizes, or their response to perturbation. Observed basin entropy $\widehat{H}_B$ summarises how sampled trajectories are distributed across reached attractors, and one-bit perturbation experiments provide a complementary measure of local recovery [10, 11, 12, 13].

These measures are affected by both local update rules and the underlying network topology [12, 14, 15].

Threshold update rules are well defined and interpretable, but they may miss regulation in which a single dominant regulator determines the target state. This form of input dominance is naturally represented by canalising update rules [16, 15, 17, 18].

Empirical regulatory networks contain activators, repressors, and dual regulators, and this balance can influence whether dynamics tend towards steady states or oscillatory behaviour [19, 20]. In the model, p_{rep} is the probability that a nonzero edge is inhibitory; we therefore refer to it as the inhibitory-edge probability.

What is less clear is how network structure changes the effects of canalising regulation and inhibitory-edge probability. Small-world networks allow network size, neighbourhood size, and rewiring to be varied systematically [21, 22].

Previous work on signed-threshold Watts–Strogatz Boolean networks examined the clustering–period association while holding the update-rule class and inhibitory-edge probability fixed [23]. The present study extends that setting by allowing depth-1 canalisation and varying inhibitory-edge probability p_{rep}. We use the controlled parameters N, κ, and p to test whether network structure modifies the effects of canalisation and inhibitory-edge probability.

The biological motivation for this extension is that regulatory systems often combine broadly acting signals with local context-dependent inputs. Gene discovery programmes in agriculture have sought individual genes whose modification could improve complex traits. A large maize biotechnology programme reported a low validation rate for genes intended to improve yield, with some genes having beneficial effects in one hybrid but neutral or negative effects in another [24]. Approaches that consider interacting gene and trait networks have therefore been proposed to improve our understanding and prediction of complex traits across genetic and environmental settings [25, 26]. Depth-1 canalisation provides a simplified Boolean model for testing how dominant regulation by one input changes attractor periods, basin summaries estimated from sampled initial states, and perturbation recovery in synthetic directed, signed Watts–Strogatz networks [12, 14, 27].

Specifically, we ask the following questions for directed, signed Watts–Strogatz Boolean networks with depth-1 canalising threshold rules:

1. How do canalising probability q_c and inhibitory-edge probability p_{rep} affect attractor period and fixed-point rate?

2. Does the effect of canalisation depend on p_{rep}?

3. How do rewiring probability p, network size N, and neighbourhood parameter κ modify these rule effects?

4. Are the period patterns accompanied by changes in basin summaries estimated from sampled initial states and recovery from one-bit perturbations?

2 Background

2.1 Threshold and canalising rule classes

The underlying network specifies which nodes can regulate a target node, but the update rule determines how those regulators are combined into the next Boolean state. This paper uses a structured rule class, rather than unrestricted truth tables, so that topology and local logic can be studied together in a controlled and interpretable way [1, 12, 15].

Threshold rules are a natural starting point for signed regulatory networks. Inputs are treated as activating or inhibitory, their signed values are summed, and the next state is determined by comparing this signed input with a threshold [16, 28]. This rule class is simple and interpretable, but it assumes that inputs combine additively. That assumption may miss regulatory settings in which one input has a dominant effect [16, 15].

Canalisation represents this dominant-input effect. A rule is canalising if one input, when it takes a particular value, can determine the output regardless of the other inputs [17, 18]. Canalising rules can reduce sensitivity, limit perturbation spread, and support more stable Boolean-network dynamics [29, 11, 12, 13].

Canalising rules have also been directly linked with fewer attractors, shorter attractor periods, and more concentrated basins [30, 31, 14].

Canalising and redundant rules are common in published biological Boolean-network models [27]. Canalising structure has also been used to identify regulatory paths that transmit control signals [32, 33].

The present study uses a depth-1 canalising construction: at most one dominant regulator can set the node state directly when the canalising condition is met. The canalising probability q_c controls how often nodes with at least one regulator are assigned this rule, while the inhibitory-edge probability p_{rep} controls the probability that a nonzero edge is inhibitory. The implementation of the canalising and fallback signed-threshold rules is specified in Sec. 4.

Dominant-input regulation is interpreted locally in this paper; the construction does not imply that one regulator controls an entire biological pathway [17, 18, 12].

2.2 Small-world construction and controlled graph parameters

We use directed, signed Watts–Strogatz networks to vary small-world structure systematically [21, 22]. The controlled graph parameters in the primary analysis are network size N, the Watts–Strogatz neighbourhood parameter κ, and rewiring probability p. At $p = 0$, the underlying graph is a regular ring lattice. For $p > 0$, each eligible local edge is rewired with probability p to another permissible endpoint. This changes the placement of non-local connections while preserving the number of edges.

Changing p changes several related graph properties at the same time, including clustering, directed path structure, and the placement of non-local connections. We therefore interpret p as the controlled rewiring parameter. We do not interpret its effect as a causal effect of clustering alone.

We record the global transitivity coefficient C and mean directed shortest path (MSP) as secondary descriptive summaries. We also retain realised average degree $\bar{k}$ as a construction check. Because the underlying Watts–Strogatz graph has $N\kappa$ edges, its mean undirected degree is $\bar{k} = 2\kappa$ by construction; $\bar{k}$ is therefore not an independent predictor. Formal definitions are given in Secs. 3.2 and 3.5.

3 Mathematical Concepts and Definitions

In this section, we introduce the fundamental concepts and definitions that will be used through-

out this paper [34, 35, 22, 36, 1, 5, 6, 8]. The simulation workflow, graph-generation procedure, parameter combinations, and implementation-specific choices are given later in the Methods section.

3.1 Graphs, adjacency, and degree

A *graph* $G = (V, E)$ has a nonempty *vertex set* V and an *edge set* E. In an undirected graph, $E \subseteq \{\{u, v\} : u, v \in V,\ u \neq v\}$; in a directed graph (a *digraph*), $E \subseteq V \times V$ with ordered pairs (u, v). The *order of* G is $N = |V|$ and the *size of* G is $m = |E|$. Throughout this paper, graphs are simple unless stated otherwise (no self-loops or parallel edges) [34, 35].

An *adjacency matrix* is $A = [a_{ij}]$. For an undirected simple graph, $a_{ij} = a_{ji} = 1$ if $\{v_i, v_j\} \in E$ and 0 otherwise. For a digraph, $a_{ij} = 1$ if $(v_i, v_j) \in E$ and symmetry is not required. For dynamical models we use a *signed adjacency* with $a_{ij} \in \{-1, 0, +1\}$ to encode activation $(+1)$ and inhibition (-1). Note that the a_{ij} values are distinct from the Boolean node values described in Sec. 3.3, which are updated at each time step. Instead, a_{ij} records the presence of any edge from v_i to v_j, and its role in the update function for node v_j.

When measuring *undirected* features (e.g., clustering), we pass to the *underlying undirected simple graph* G^u with adjacency $U = [u_{ij}]$ defined by

$$u_{ij} = \begin{cases} 1, & \text{if } a_{ij} \neq 0 \text{ or } a_{ji} \neq 0, \\ 0, & \text{otherwise,} \end{cases} \qquad u_{ii} = 0 \text{ for all } i,$$

and then treat G^u as a simple graph (so directions and signs are both ignored and parallel edges are not allowed). Unless otherwise noted, any undirected network statistic is computed on G^u constructed from A as above [35, 22].

The *degree of vertex* v_i in an undirected graph is $\deg(v_i) = \sum_j u_{ij}$ and equals the size of the *neighbourhood* $N(v_i) = \{v_j : \{v_i, v_j\} \in E\}$. In a digraph, the *in-degree* and *out-degree* are

$$\begin{aligned} \deg_{\text{in}}(v_i) &= \sum_j \mathbf{1}[a_{ji} \neq 0], \\ \deg_{\text{out}}(v_i) &= \sum_j \mathbf{1}[a_{ij} \neq 0], \end{aligned} \tag{1}$$

where $\mathbf{1}[\cdot]$ denotes the indicator, equal to 1 when the condition holds and 0 otherwise. We write the *total degree of vertex* v_i as $\deg_{\text{tot}}(v_i) = \deg_{\text{in}}(v_i) + \deg_{\text{out}}(v_i)$ (in an undirected graph, $\deg_{\text{tot}}(v_i) = \deg(v_i)$), and define the *average degree* as $\bar{k} = \frac{1}{N}\sum_{i=1}^{N} \deg_{\text{tot}}(v_i)$ (so $\bar{k} = 2m/N$ for simple graphs) [34].

Regulatory-network notation used in this paper. In this paper, the regulatory system is represented by a directed signed graph $G = (V, E)$, with $V = \{v_1, \ldots, v_N\}$ and $E \subseteq V \times V$. Its signed adjacency matrix is $A = [a_{ij}]_{i,j=1}^{N}$, where

$$a_{ij} = \begin{cases} +1, & \text{if } v_i \to v_j \text{ is activating,} \\ -1, & \text{if } v_i \to v_j \text{ is inhibitory,} \\ 0, & \text{if there is no edge from } v_i \text{ to } v_j. \end{cases}$$

Thus, i is the source vertex and j is the target vertex [3, 16, 19]. For vertex v_j, the set of regulators, or in-neighbours, is

$$N^-(v_j) = \{\, v_i : a_{ij} \neq 0 \,\}. \tag{2}$$

Because each undirected Watts–Strogatz edge is oriented once in the graph-generation procedure used here (Sec. 3.5), $\deg_{\text{tot}}(v_i) = \deg_{G^u}(v_i)$. Therefore, $\bar{k}$ measures the overall realised connectivity of the underlying undirected graph. The mean number of incoming regulators is $m/N = \bar{k}/2 = \kappa$, while the realised in-degree of each vertex depends on edge orientation.

3.2 Paths, distance, clustering, and path-based measures

A *walk* of *length* ℓ_{w} is a sequence $(u_0, \ldots, u_{\ell_{\text{w}}})$ with adjacent consecutive vertices; a *path* is a walk with no repeated vertices [34]. In a digraph, we write $u \Rightarrow v$ to denote that there exists a directed path from u to v. In an undirected simple graph, a

(simple) *cycle* is a closed walk of length at least 3 whose vertices are all distinct except the first and last. A *3-cycle* (a *triangle*) is a cycle of length 3 (in a digraph, edges of the cycle must respect orientation). Directed cycles can also have length 2, and a self-loop gives a cycle of length 1 when self-loops are allowed.

The *distance* $d(u, v)$ is the length of a shortest path from u to v (respecting edge directions in digraphs). The *diameter of* G is the maximum finite distance [22].

For clustering we count *triangles* (3-cycles) and *connected triples* (wedges) on the underlying undirected simple graph G^u. A *connected triple (wedge)* is a path of length 2, $u-v-w$, in G^u, with $u \neq w$. The neighbour pair $\{u, w\}$ is unordered, so each wedge is counted once for its central vertex v. Writing T for the number of triangles and Λ for the number of connected triples, the global clustering coefficient (transitivity) C is defined as

$$C = \begin{cases} \dfrac{3T}{\Lambda}, & \Lambda > 0, \\ 0, & \Lambda = 0, \end{cases} \quad \text{with } C \in [0, 1], \tag{3}$$

which is the fraction of wedges that are closed into triangles [22, 36, 37].

We use the mean *directed* shortest path (MSP), defined as

$$\mathrm{MSP} = \begin{cases} \dfrac{1}{|\mathcal{R}|} \displaystyle\sum_{(u,v)\in\mathcal{R}} d(u, v), & |\mathcal{R}| > 0, \\ 0, & |\mathcal{R}| = 0, \end{cases} \tag{4}$$

where

$$\mathcal{R} = \{(u, v) \in V \times V : \ u \neq v, \ u \Rightarrow v \text{ in } G\}, \tag{5}$$

and $d(u, v)$ is the length of a shortest *directed* path from u to v. Thus, G need not be (strongly) connected; the average is taken only over ordered pairs that are reachable by a directed path (i.e., pairs in $\mathcal{R}$) [22]. The value 0 when $|\mathcal{R}| = 0$ is an assigned value for graphs with no reachable ordered pairs, and should not be interpreted as a zero path length.

3.3 Boolean networks, attractors, and basins

Given a graph $G = (V, E)$ with $|V| = N$, we associate a Boolean state to each vertex at each discrete time $t \in \mathbb{Z}_{\geq 0}$. The *state vector* is

$$S(t) = (s_1(t), \ldots, s_N(t)) \in \{0, 1\}^N,$$

with a chosen initial condition $S(0) \in \{0, 1\}^N$. A Boolean network on G is the deterministic map

$$\begin{aligned} &F : \{0, 1\}^N \to \{0, 1\}^N, \\ &S(t) \mapsto F(S(t)) = \Big(f_1(S(t)), \ldots, f_N(S(t))\Big), \end{aligned} \tag{6}$$

where each coordinate function $f_j : \{0, 1\}^N \to \{0, 1\}$ depends only on the states of the in-neighbours of the vertex v_j in G [5, 6]. In Eq. (6), $\to$ specifies the domain and codomain of F, while $\mapsto$ means "maps to" and shows how the state $S(t)$ is mapped to $F(S(t))$. The synchronous evolution is then

$$S(t{+}1) = F\Big(S(t)\Big).$$

An *update scheme* specifies when node states are updated. In the *synchronous* scheme, all nodes update simultaneously at each integer time step according to Eq. (6). Asynchronous variants (e.g., random-order or general-asynchronous) update subsets or single nodes per step; in this study we focus on synchronous updates [6, 38].

An *update rule* specifies the coordinate functions f_j used in Eq. (6) and, together with the update scheme, determines the next state $S(t{+}1)$ from $S(t)$ [6]. A widely used rule in signed regulatory models is the *signed–threshold rule*,

$$s_j(t{+}1) = \mathbf{1}\left(\sum_{i=1}^{N} a_{ij}\, s_i(t) \ \circ \ \theta_j \right), \tag{7}$$

where $a_{ij} \in \{-1, 0, +1\}$, $\theta_j \in \mathbb{R}$ is a node-specific threshold, and the comparison symbol $\circ \in \{>, \geq\}$; in this study we use the strict comparator "$>$" throughout (see Sec. 4) [6, 3, 39].

An *attractor* is a minimal set $\mathcal{A} = \{S_0, \ldots, S_{L-1}\} \subseteq \{0, 1\}^N$ such that $F(S_r) = S_{(r+1) \bmod L}$ for all $r \in \{0, \ldots, L-1\}$. Equivalently, $F^L(S_r) = S_r$ with no smaller positive

period. The *period* is $L \in \{1, 2, \dots\}$ (a fixed point is the case $L = 1$). The *state transition graph* places a directed edge $S \to F(S)$ on the 2^N states (out-degree 1 per state); attractors are precisely the directed cycles (with fixed points as 1-cycles) [6, 8].

From a given initial state $S(0)$, the trajectory $S(0), S(1), \dots$ eventually repeats because $\{0,1\}^N$ is finite. The *transient length* from $S(0)$ is

$$T_{\mathrm{tr}} = \min\{t \geq 0 : \ S(t) \in \mathcal{A}\},$$

i.e., the first time the trajectory enters the repeating cycle.

Basins of attraction. For an attractor $\mathcal{A}$, the *basin of attraction* is the set of initial states whose trajectories eventually enter $\mathcal{A}$. Formally,

$$\mathcal{B}(\mathcal{A}) = \{\, S \in \{0,1\}^N : \exists\, t \geq 0,\ F^t(S) \in \mathcal{A} \,\}. \tag{8}$$

When the full state space is considered, the basins of all attractors partition $\{0,1\}^N$: every initial state belongs to the basin of exactly one attractor. If the attractors are $\mathcal{A}_1, \dots, \mathcal{A}_K$, the corresponding basin proportions are

$$\pi_r = \frac{|\mathcal{B}(\mathcal{A}_r)|}{\sum_{s=1}^{K} |\mathcal{B}(\mathcal{A}_s)|}, \qquad r = 1, \dots, K, \tag{9}$$

and the *basin entropy* is

$$H_B = -\sum_{r=1}^{K} \pi_r \log \pi_r. \tag{10}$$

Here and throughout, log denotes the natural logarithm [10].

Hamming distance. The *Hamming distance* between two states $S, \widetilde{S} \in \{0,1\}^N$ is

$$D_{\mathrm{H}}(S, \widetilde{S}) = \sum_{i=1}^{N} \mathbf{1}[s_i \neq \widetilde{s}_i], \tag{11}$$

and the corresponding Hamming fraction is

$$h(S, \widetilde{S}) = \frac{1}{N} D_{\mathrm{H}}(S, \widetilde{S}). \tag{12}$$

The normalised form is used when perturbation size is reported as a fraction of nodes rather than as a raw count.

Period summaries from many initial states. When summarising outcomes over many initial states, we report the *arithmetic mean period* and *mean log period*. From $n_{\mathrm{traj}} > 0$ detected trajectories with periods L_r,

$$\bar{L} = \frac{1}{n_{\mathrm{traj}}} \sum_{r=1}^{n_{\mathrm{traj}}} L_r, \tag{13}$$

and

$$Y = \frac{1}{n_{\mathrm{traj}}} \sum_{r=1}^{n_{\mathrm{traj}}} \log L_r. \tag{14}$$

The geometric mean period is $L_{\mathrm{geo}} = \exp(Y)$, and a difference ΔY corresponds to a multiplicative factor $e^{\Delta Y}$ on L_{geo} [8, 40].

3.4 Depth-1 canalising rules

For node v_j, the *signed input* at time t is

$$I_j(t) = \sum_{i=1}^{N} a_{ij}\, s_i(t). \tag{15}$$

Using the strict comparator adopted in this paper, the signed–threshold rule in Eq. (7) may be written as

$$s_j(t{+}1) = \mathbf{1}[I_j(t) > \theta_j]\,.$$

Threshold rules are useful because they provide a simple signed approximation to regulatory logic [16, 28, 15].

To add canalisation, let

$$z_j \in \{0,1\}$$

indicate whether node v_j has a canalising rule. If $z_j = 1$ and $N^-(v_j) \neq \emptyset$, one regulator

$$v_{r(j)} \in N^-(v_j)$$

is designated as the dominant regulator. Here, $r(j)$ is the index of that regulator. If $N^-(v_j) = \emptyset$, we set $z_j = 0$, and no dominant regulator is assigned. This regulator has a canalising input $\alpha_j \in \{0,1\}$ and a canalised output $b_j \in \{0,1\}$. The canalising condition is

$$z_j = 1 \qquad \text{and} \qquad s_{r(j)}(t) = \alpha_j. \tag{16}$$

If this condition is met, node v_j is forced to b_j. Otherwise, it follows a fallback rule f_j^{fb}. In general form,

$$s_j(t{+}1) = \begin{cases} b_j, & \text{if } z_j = 1 \text{ and } s_{r(j)}(t) = \alpha_j, \\ f_j^{\mathrm{fb}}\big(S(t)\big), & \text{otherwise.} \end{cases} \tag{17}$$

In the present paper, the fallback rule f_j^{fb} is a signed-threshold rule. Thus, the dominant input has priority only when its canalising condition is met; otherwise, the node follows the fallback signed-threshold rule. Here, depth-1 refers to the use of at most one designated dominant regulator before the rule falls back to signed-threshold updating [17, 18, 31, 14]. The implementation-specific choices for α_j, b_j, the ordinary threshold θ_j, and the fallback threshold θ_j^{fb} used by f_j^{fb} are given in the Methods section.

3.5 Watts–Strogatz graph model

Fix an integer $N \geq 3$ and an integer $\kappa \in \{1, \ldots, \lfloor (N-1)/2 \rfloor\}$, and let $p \in [0, 1]$. Let $V = \{0, 1, \ldots, N-1\}$ and for $u, v \in V$ with $u \neq v$ define the circular distance

$$\delta(u, v) = \min\Big\{|u - v|,\ N - |u - v|\Big\}.$$

The ring lattice $\mathcal{L}(N, \kappa)$ has edge set

$$E_0 = \Big\{\{u, v\} \subset V :\ 1 \leq \delta(u, v) \leq \kappa\Big\},$$

so every vertex in the initial ring lattice has undirected degree $\deg(u) = 2\kappa$, where κ is the ring-lattice parameter. Construct the undirected WS graph $H = \mathrm{WS}(N, \kappa, p)$ by considering each $\{u, v\} \in E_0$ once and independently deciding whether to rewire it: with probability p replace $\{u, v\}$ by $\{u, w\}$, where w is drawn uniformly from $V \setminus (\{u\} \cup N_H(u))$ at the time of rewiring (avoids self-loops and multi-edges); otherwise keep $\{u, v\}$. Here, $N_H(u)$ is the current neighbourhood of u. If no permissible endpoint is available, the edge is retained. This preserves $m = |E(H)| = N\kappa$ and hence the mean (undirected) degree $\bar{k} = 2m/N = 2\kappa$ [21, 22, 36].

The *directed* WS graph $G_{\mathrm{WS}} = \overrightarrow{\mathrm{WS}}(N, \kappa, p)$ is obtained by orienting each undirected edge of H independently and uniformly at random:

$$\begin{aligned} &\mathbb{P}((u, v) \in E(G_{\mathrm{WS}}) \,|\, \{u, v\} \in E(H)) = \tfrac{1}{2}, \\ &\mathbb{P}((v, u) \in E(G_{\mathrm{WS}}) \,|\, \{u, v\} \in E(H)) = \tfrac{1}{2}. \end{aligned} \tag{18}$$

Conditioned on H,

$$\begin{aligned} \deg_{\mathrm{in}}^{G_{\mathrm{WS}}}(v) &\sim \mathrm{Binomial}\Big(\deg_H(v), \tfrac{1}{2}\Big), \\ \deg_{\mathrm{out}}^{G_{\mathrm{WS}}}(v) &\sim \mathrm{Binomial}\Big(\deg_H(v), \tfrac{1}{2}\Big), \end{aligned} \tag{19}$$

so

$$\mathbb{E}\Big[\deg_{\mathrm{in}}^{G_{\mathrm{WS}}}(v) \,\Big|\, H\Big] = \mathbb{E}\Big[\deg_{\mathrm{out}}^{G_{\mathrm{WS}}}(v) \,\Big|\, H\Big] = \tfrac{1}{2}\, \deg_H(v). \tag{20}$$

3.6 Graph-level summaries and perturbation measures

For graph-level summaries, n_{traj} denotes the number of valid trajectories retained for one graph-level unit: those that detect an attractor before the cap specified in Sec. 4.4. In the graph-replicate period design, the unit is a graph–rule replicate; in the basin-and-perturbation design, the unit is a fixed Boolean system. Threshold handling for the two designs is specified in Sec. 4.3.

If the retained periods are $L_1, \ldots, L_{n_{\mathrm{traj}}}$, the graph-level summaries $\bar{L}$, Y, and L_{geo} are computed as defined in Eqs. (13) and (14). If $n_{\mathrm{traj}} = 0$ in the graph-replicate period design, these summaries are undefined and the graph-level row is excluded from the period analysis.

The graph-level *fixed-point rate* is the proportion of detected runs with $L_r = 1$:

$$\mathrm{FixedRate} = \frac{1}{n_{\mathrm{traj}}} \sum_{r=1}^{n_{\mathrm{traj}}} \mathbf{1}[L_r = 1], \tag{21}$$

for $n_{\mathrm{traj}} > 0$. The graph-level *detection rate* is the proportion of sampled trajectories in which an attractor is detected before the simulation cap. It is reported separately as a measure of detection completeness and is not part of the period summaries.

If $\mathcal{A}_1, \ldots, \mathcal{A}_{K_{\mathrm{obs}}}$ are the attractors reached by the detected sampled runs in one fixed Boolean

system, with $K_{\text{obs}} > 0$, let $\hat{\pi}_r$ be the fraction of detected sampled runs that reach attractor $\mathcal{A}_r$. The largest observed basin fraction is

$$B_{\max} = \max_{1 \le r \le K_{\text{obs}}} \hat{\pi}_r, \tag{22}$$

and the observed basin entropy is

$$\widehat{H}_B = -\sum_{r=1}^{K_{\text{obs}}} \hat{\pi}_r \log \hat{\pi}_r. \tag{23}$$

These are summaries estimated from repeated sampled initial states on a fixed deterministic update map rather than exact full-state-space quantities.

For perturbation analysis, within a fixed Boolean system, let S be a state on an attractor $\mathcal{A}$, and let $\widetilde{S}$ be a one-bit perturbation of S, so that

$$D_{\text{H}}(S, \widetilde{S}) = 1, \qquad h(S, \widetilde{S}) = \frac{1}{N}. \tag{24}$$

The return-to-same-attractor event occurs when the perturbed trajectory re-enters the original attractor $\mathcal{A}$ within the chosen return window. If F^t denotes the t-fold iterate of the update map, the *return time* is

$$\tau_{\text{ret}} = \min\{\, t \ge 1 : F^t(\widetilde{S}) \in \mathcal{A} \,\}, \tag{25}$$

provided such a time exists within that window.

For each perturbation trial i, the restricted return time is

$$T_i = \begin{cases} \tau_{\text{ret},i}, & \text{if a return is observed,} \\ 2000, & \text{otherwise.} \end{cases} \tag{26}$$

Here, a return is observed when the perturbed trajectory re-enters the original attractor within the 2000-update window. The restricted mean return time is the mean of T_i across the perturbation trials for one fixed Boolean system.

To track perturbation spread over time, we compare the unperturbed and perturbed trajectories after t synchronous updates. The *Hamming fraction at horizon t* is

$$h_t = \frac{1}{N} D_{\text{H}}\Big(F^t(S), F^t(\widetilde{S})\Big). \tag{27}$$

The initial perturbation has Hamming fraction $h_0 = 1/N$ [13, 12, 14].

4 Methods

4.1 Simulation overview

The study uses two simulation datasets. The graph-replicate period design generates multiple graph–rule replicates for each controlled parameter combination and is used for the observed period and fixed-point summaries and the primary period model. The fixed-system basin-and-perturbation design uses a reduced parameter grid to estimate basin summaries from sampled initial states and recovery after one-bit perturbations. Parameter grids, sample sizes, threshold handling, and recorded outcomes are described below.

4.2 Graph generation and edge signs

The underlying graph is the directed Watts–Strogatz graph $G_{\text{WS}} = \overrightarrow{\text{WS}}(N, \kappa, p)$ defined in Sec. 3.5. The simulation grid uses the degree-control input d, which is mapped to the WS ring-lattice parameter by

$$\kappa = \max\left(\left\lfloor \frac{d}{2} \right\rfloor, 1\right). \tag{28}$$

After orientation as in Eq. (18), each nonzero edge is assigned a sign independently:

$$a_{ij} = \begin{cases} -1, & \text{with probability } p_{\text{rep}}, \\ +1, & \text{with probability } 1 - p_{\text{rep}}, \end{cases} \tag{29}$$

Thus, p_{rep} is the probability that a nonzero edge is inhibitory.

For each graph, we compute the average degree $\bar{k}$, clustering coefficient C (Eq. (3)), and mean directed shortest path MSP (Eq. (4)).

4.3 Rule assignment and threshold construction

The update rule at each node is either a signed-threshold rule or a depth-1 canalising rule with a fallback signed-threshold rule, as described in Sec. 3.4. The parameter q_c controls the probability that a canalising rule is used at each node with at least one in-neighbour.

For each node v_j with $N^-(v_j) \neq \emptyset$, we independently assign a canalising indicator $z_j \in \{0, 1\}$, with

$$\Pr(z_j = 1) = q_c.$$

Nodes with no in-neighbours are assigned $z_j = 0$. Within each graph–rule replicate, the graph structure, edge signs, canalising assignments, dominant regulators, and canalised outputs are fixed across the sampled initial states.

Threshold perturbations are handled according to the simulation design. In the graph-replicate period design, a new vector $(\varepsilon_1, \ldots, \varepsilon_N)$ is drawn for each trajectory. In the basin-and-perturbation design, one vector is drawn per fixed Boolean system and retained across all sampled initial states and perturbation trials. In both cases, $\varepsilon_j \sim \mathcal{N}(0, \sigma^2)$ with $\sigma = 10^{-4}$. The perturbation ε_j prevents exact ties.

If $z_j = 0$, node v_j uses the signed-threshold rule with threshold

$$\theta_j = \frac{1}{2} \sum_{i=1}^{N} a_{ij} + \varepsilon_j.$$

If $z_j = 1$, one in-neighbour $v_{r(j)} \in N^-(v_j)$ is chosen uniformly at random as the dominant regulator. The canalising input is fixed at $\alpha_j = 1$. The canalised output is determined by the sign of the dominant edge:

$$b_j = \begin{cases} 1, & \text{if } a_{r(j),j} = +1, \\ 0, & \text{if } a_{r(j),j} = -1. \end{cases}$$

Thus, within the local update rule, an active dominant activator forces node v_j to 1, while an active dominant inhibitor forces node v_j to 0.

When the canalising condition is not met, the node follows a fallback signed-threshold rule with fallback threshold

$$\theta_j^{\mathrm{fb}} = \frac{1}{2} \left(\sum_{i=1}^{N} a_{ij} - a_{r(j),j} \right) + \varepsilon_j.$$

The signed input $I_j(t)$ is defined in Eq. (15). In the fallback branch, $s_{r(j)}(t) = 0$, so the dominant regulator contributes zero to $I_j(t)$, giving $I_j(t) = \sum_{i \neq r(j)} a_{ij} s_i(t)$, while θ_j^{fb} is centred on the remaining signed regulators.

The full update rule used in the simulations is therefore

$$s_j(t+1) = \begin{cases} b_j, & z_j = 1,\ s_{r(j)}(t) = 1, \\ \mathbf{1}\left[I_j(t) > \theta_j^{\mathrm{fb}} \right], & z_j = 1,\ s_{r(j)}(t) = 0, \\ \mathbf{1}[I_j(t) > \theta_j], & z_j = 0. \end{cases}$$

The three update-rule cases are illustrated in Fig. 1.

4.4 Trajectory-based attractor detection

All simulations use synchronous updates. For each run, the initial state $S(0)$ is sampled independently with

$$\Pr\{s_i(0) = 1\} = 0.5.$$

For each sampled initial state, the reached attractor is detected using a compiled `Rcpp` implementation. Starting from the initial state, the system is updated one step at a time. Each visited state is converted to a binary string and stored in a hash table. When a state repeats, the repeated segment is returned as the attractor. Its number of distinct states is the period L [8, 9].

The detector records the period, attractor states, and an attractor identifier that does not depend on which cycle state is stored first. Recurrence must occur within `max_iters` $= 10^6$ updates; runs exceeding this cap are recorded as not found. Detection is exact along each sampled trajectory.

4.5 One-bit perturbation trials

One-bit perturbation trials are used only in the fixed-system basin-and-perturbation design. In each trial, an attractor is first detected from a sampled initial state. As a fixed convention, the first stored state S of the detected attractor cycle is used as the perturbation base state. One node is then selected uniformly at random and flipped to form $\widetilde{S}$, giving the one-bit perturbation defined in Eq. (24). Thus, perturbation trials sample one stored phase of each detected attractor rather than averaging uniformly over all phases of the attractor cycle.

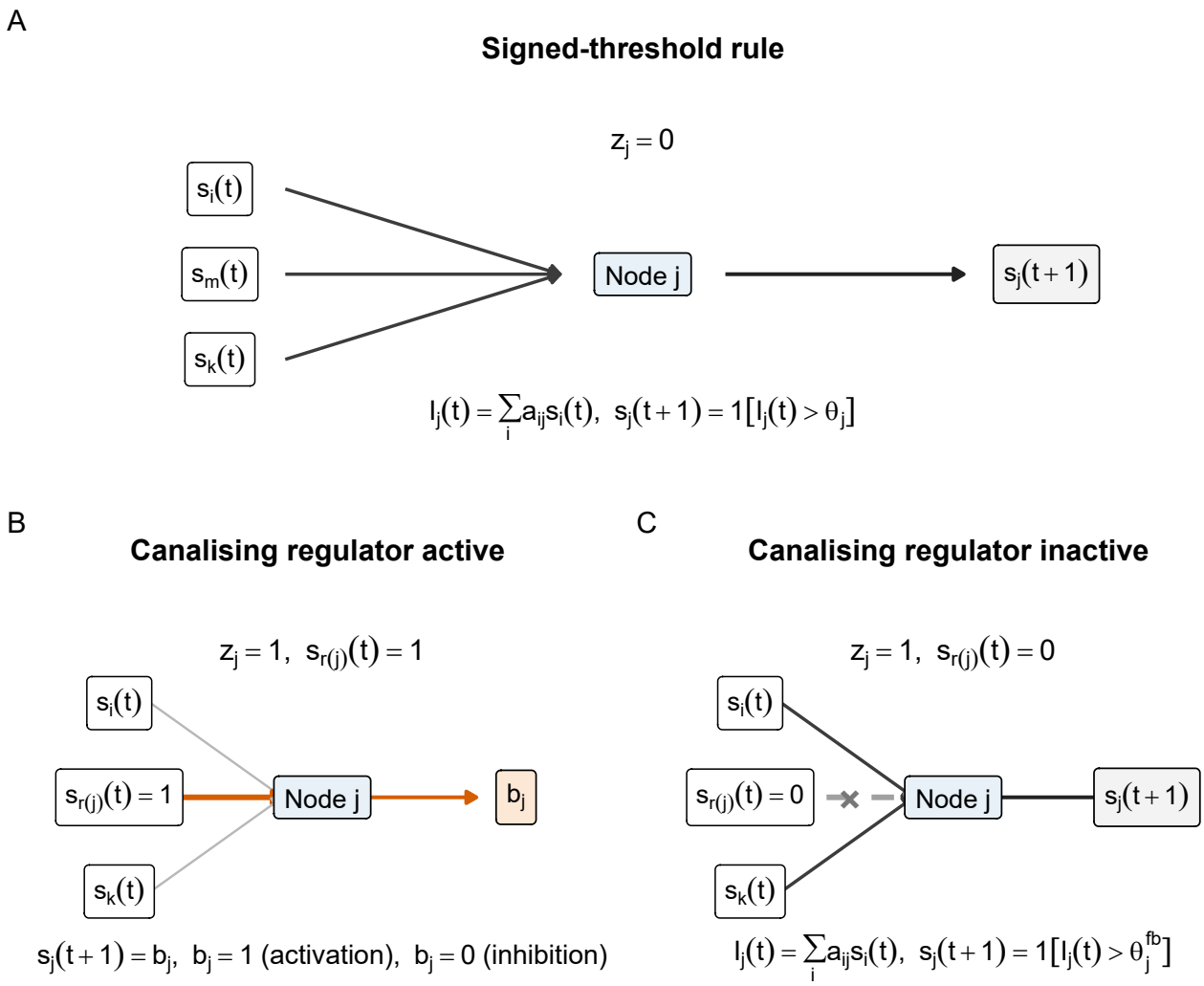


Figure 1: Examples of the update-rule scenarios. A node with $z_j = 0$ uses the signed-threshold rule. For a node with $z_j = 1$, an active dominant input fixes the target state according to the sign of the dominant edge; when the dominant input is inactive, the node uses the fallback signed-threshold rule.

The perturbed trajectory is then followed for a 2000-step return window. A trial is recorded as a return if the perturbed trajectory re-enters the original attractor within that window. Otherwise, it is recorded as a non-return within the window. A non-return does not prove that return is impossible; it only means that return was not observed before the return cap.

For each trial, we record whether and when the trajectory returns to the original attractor and the Hamming fraction h_t for $0 \leq t \leq 25$. The values h_1, h_{10}, and h_{25} summarise perturbation spread [11, 13, 12, 14].

4.6 Simulation datasets and recorded quantities

Graph-replicate period design. The simulations use

$$\begin{aligned} N &\in \{10, 20, \ldots, 100\}, \\ d &\in \{1, \ldots, \lfloor N/10 \rfloor\}, \\ p &\in \{0.01, 0.05, 0.10, 0.20, 0.40, 0.60\}, \\ p_{\text{rep}} &\in \{0.10, 0.24, 0.30, 0.41, 0.50\}, \\ q_c &\in \{0, 0.25, 0.50, 0.75, 1\}. \end{aligned}$$

The simulation design contained 8,250 $(N, d, p, q_c, p_{\text{rep}})$ cells. For each original cell, 100 independently generated graph–rule replicates were simulated from 25 initial states, giving 825,000 graph-level replicates.

For the controlled-parameter analysis, we applied the mapping in Eq. (28). This produced 3,900 unique $(N, \kappa, p, q_c, p_{\text{rep}})$ controlled-parameter cells. Because several values of d can map to the same κ, these cells contain different numbers of graph replicates. The primary graph-level model and the observed period and fixed-point summaries treat each independently generated graph–rule replicate as one equally contributing observation.

Basin-and-perturbation design. This design uses a reduced parameter grid:

$$N \in \{20, 60, 100\}, \quad p \in \{0.01, 0.10, 0.60\},$$

$$p_{\text{rep}} \in \{0.30, 0.50\}, \qquad q_c \in \{0, 0.25, 0.50, 0.75, 1\}.$$

For each N, we use representative values of the degree-control input:

$$d \in \left\{1, \left\lceil \frac{\lfloor N/10 \rfloor}{2} \right\rceil, \left\lfloor \frac{N}{10} \right\rfloor \right\}, \tag{30}$$

after removing duplicates. This gives $d \in \{1, 2\}$ for $N = 20$, $d \in \{1, 3, 6\}$ for $N = 60$, and $d \in \{1, 5, 10\}$ for $N = 100$.

For each parameter combination, 30 Boolean systems are generated. Basin summaries use 200 initial states per system, and perturbation summaries use 30 one-bit perturbation trials per system. This gives 7,200 fixed Boolean systems, with 720 systems in each of the ten (p_{rep}, q_c) combinations. The perturbation return window is defined in Sec. 4.5; it is separate from the attractor-detection cap in Sec. 4.4.

Basin summaries include the largest observed basin fraction, the number of attractors reached from sampled initial states, and observed basin entropy. Perturbation recovery is summarised by return probability, restricted mean return time over the 2000-update window, return time among successful returns, and Hamming fractions at the specified update horizons.

4.7 Statistical modelling

For each graph–rule replicate g, the period response Y_g is the mean log period across its valid detected trajectories, as defined in Eq. (14); $\exp(Y_g)$ is the corresponding geometric mean period.

The primary model estimates the effects of q_c and p_{rep} on mean log period and tests whether these effects vary with the controlled graph parameters N, κ, and p. Clustering, realised average degree, and MSP are not included as primary predictors. The candidate models were Gaussian additive models with an identity link, fitted in R using the `mgcv` package. Tensor-product smooths were used for the specified continuous interactions.

Four controlled-parameter models were compared by maximum likelihood using the 3,900 controlled-parameter cell means. Each cell mean was accompanied by the number of graph replicates it represented, and these counts were used so that each underlying graph replicate contributed equally during candidate-model comparison. The models progressively added the rewiring–rule interaction, the specified pairwise smooth interactions, and the targeted $\kappa \times q_c \times p_{\text{rep}}$ interaction. Model comparison and grouped cross-validation selected the model containing the targeted three-way interaction as the primary model. The candidate-model sequence and comparison results are reported in Supplementary Tables S5 and S6.

The primary model is

$$\begin{aligned} Y_g = \beta_0 &+ \mathrm{te}(N_{c,g}, \kappa_{c,g}) \\ &+ p_{f,g} \times q_{c,f,g} \times p_{\mathrm{rep},f,g} \\ &+ \mathrm{ti}(N_{c,g}, \widetilde{p}_g) + \mathrm{ti}(\kappa_{c,g}, \widetilde{p}_g) \\ &+ \mathrm{ti}(N_{c,g}, \widetilde{q}_{c,g}) + \mathrm{ti}(\kappa_{c,g}, \widetilde{q}_{c,g}) \\ &+ \mathrm{ti}(N_{c,g}, \widetilde{p}_{\mathrm{rep},g}) + \mathrm{ti}(\kappa_{c,g}, \widetilde{p}_{\mathrm{rep},g}) \\ &+ \mathrm{ti}(\kappa_{c,g}, \widetilde{q}_{c,g}, \widetilde{p}_{\mathrm{rep},g}) + \xi_g. \end{aligned} \tag{31}$$

Here g indexes a graph–rule replicate, β_0 is the intercept, the subscript c denotes a centred continuous graph variable, the subscript f denotes a factor-coded variable, a tilde denotes a centred numerical version of a controlled grid variable, and ξ_g denotes the model residual. The function te represents the full smooth joint relationship between its variables, whereas ti represents a smooth interaction after the corresponding lower-order effects have been included. The symbol $\times$ denotes the full factor interaction, including its lower-order terms. Rewiring probability p, canalising probability q_c, and inhibitory-edge probability p_{rep} are factor-coded in the controlled-grid interaction and enter the tensor-product smooths as centred numerical variables.

The primary model in Eq. (31) was refitted to all 825,000 graph-level replicates using fast restricted maximum likelihood. Model performance was evaluated by five-fold grouped cross-validation, with complete controlled-parameter cells assigned to folds so that rows from the same cell did not occur in both training and test data.

Contrasts are averaged equally over parameter combinations present in the simulations; we refer to these as standardised contrasts. Differences on the Y scale are exponentiated to obtain ratios of geometric mean periods. Where multiplicity adjustment is reported, p-values are adjusted using the Holm method within the stated contrast family; other endpoint p-values are unadjusted. The basin and perturbation outcomes are first summarised within each fixed Boolean system. Endpoint differences between $q_c = 1$ and $q_c = 0$ are then compared across systems using Welch confidence intervals and tests. These are descriptive comparisons, and no multiplicity adjustment is applied to the basin or perturbation endpoint comparisons.

Throughout the paper, unless stated otherwise, all intervals reported in the text and tables and all bands or error bars shown in figures are 95% confidence intervals.

5 Results

We first tested how canalising probability q_c and inhibitory-edge probability p_{rep} affected attractor period, and then whether those effects changed with rewiring probability p, network size N, and the Watts–Strogatz neighbourhood parameter κ. We finally examined whether the period patterns were accompanied by changes in basin summaries estimated from sampled initial states and recovery from one-bit perturbations. Period-model results are reported on the mean log period scale; exponentiated contrasts give ratios of geometric mean periods.

5.1 Canalisation effects on attractor period depend on inhibitory-edge probability

The observed graph-level summaries were calculated so that each independently generated graph–rule replicate contributed equally, and were then averaged over the simulated N, κ, and p values. Increasing q_c from 0 to 1 reduced the observed geometric mean period by 7.4% at $p_{\mathrm{rep}} = 0.10$, and by 42.8%, 47.7%, 47.0%, and 42.5% at $p_{\mathrm{rep}} = 0.24$, 0.30, 0.41, and 0.50, respectively (Fig. 2A). The $p_{\mathrm{rep}} = 0.10$ curve was the only case that did not decrease monotonically: the period increased slightly between $q_c = 0$ and $q_c = 0.25$, then decreased as q_c increased further.

From $q_c = 0$ to $q_c = 1$, the observed fixed-point rate decreased at every inhibitory-edge probability, with endpoint differences ranging from -0.054 (95% CI $[-0.060, -0.048]$) at $p_{\mathrm{rep}} = 0.24$ to -0.130 (95% CI $[-0.136, -0.124]$) at $p_{\mathrm{rep}} = 0.50$ (Fig. 2B). Thus, the shorter periods were not explained by an increase in the proportion of detected trajectories reaching fixed points.

The primary model confirmed that the magnitude of the period effect of canalisation depended

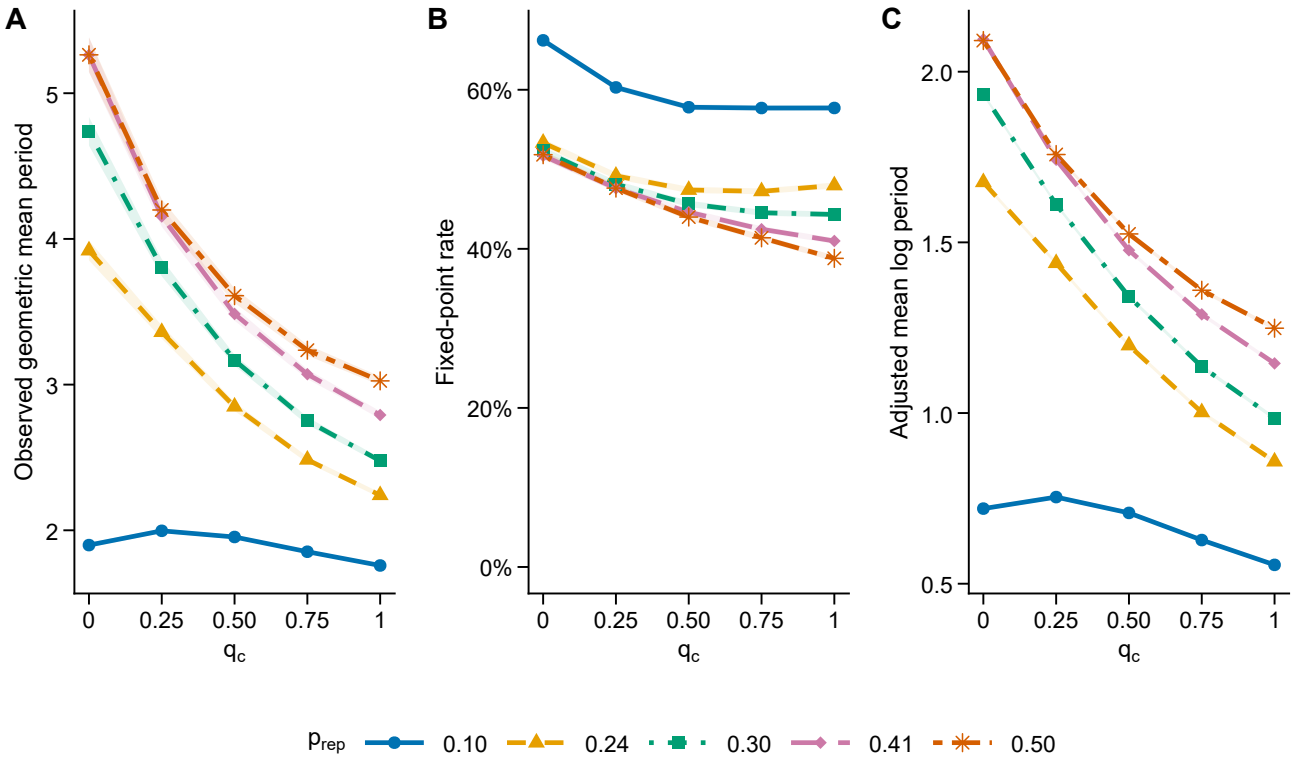


Figure 2: Observed and adjusted effects of canalisation and inhibitory-edge probability. Panel A shows the observed geometric mean period, panel B shows the observed fixed-point rate, and panel C shows the adjusted mean log period from the primary model, across q_c and p_{rep}. Each independently generated graph–rule replicate contributes equally to panels A and B. Panel C predictions are averaged equally over controlled-parameter combinations present in the simulations.

on p_{rep} (Fig. 2C). At $p_{\text{rep}} = 0.10$, the adjusted $q_c = 1$ versus $q_c = 0$ contrast was $\Delta Y = -0.165$ (95% CI $[-0.174, -0.156]$), equivalent to a 15.2% shorter geometric mean period. The corresponding reductions at $p_{\text{rep}} = 0.24$, 0.30, 0.41, and 0.50 were 55.9%, 61.3%, 61.3%, and 56.9%, respectively (all Holm-adjusted $p < 0.001$). The slight increase at low canalisation was retained after adjustment: at $p_{\text{rep}} = 0.10$, $q_c = 0.25$ gave a 3.4% longer period than $q_c = 0$ (95% CI for ΔY, $[0.025, 0.042]$).

Inhibitory-edge probability also had a large adjusted effect. Relative to $p_{\text{rep}} = 0.50$, $p_{\text{rep}} = 0.10$ reduced the geometric mean period by 74.6% when $q_c = 0$ ($\Delta Y = -1.371$, 95% CI $[-1.380, -1.362]$) and by 50.0% when $q_c = 1$ ($\Delta Y = -0.693$, 95% CI $[-0.702, -0.685]$). Thus, canalisation narrowed, but did not remove, the separation between the lowest and highest inhibitory-edge probabilities. The fitted model explained 80.8% of graph-level deviance; five-fold grouped cross-validation gave $R^2 = 0.804$ and RMSE = 0.560, close to the in-sample values of 0.808 and 0.554, respectively.

5.2 Rewiring modifies canalisation effects across inhibitory-edge probabilities

The canalisation pattern across inhibitory-edge probabilities occurred at every simulated rewiring probability (Supplementary Table S11), but its magnitude changed with p. Supplementary Fig. S2 shows representative low, intermediate, and high rewiring probabilities. For $p_{\text{rep}} = 0.24$–0.50, the $q_c = 1$ versus $q_c = 0$ reduction increased from 44.4%–49.9% at $p = 0.01$ to 65.3%–70.4%

at $p = 0.60$. The lowest inhibitory-edge probability again behaved differently: at $p_{\text{rep}} = 0.10$, the reduction weakened from 22.1% at $p = 0.01$ to 11.8% at $p = 0.60$.

After averaging predictions equally over the simulated N–κ combinations, increasing rewiring from $p = 0.01$ to $p = 0.60$ shortened the adjusted period in every (q_c, p_{rep}) combination, although the magnitude depended on q_c and p_{rep} (Fig. 3; complete endpoint contrasts are reported in Supplementary Table S12). At $p_{\text{rep}} = 0.30$, the rewiring contrast was $\Delta Y = -0.099$ (95% CI $[-0.119, -0.078]$), or a 9.4% reduction, when $q_c = 0$; it was $\Delta Y = -0.624$ (95% CI $[-0.645, -0.603]$), or a 46.4% reduction, when $q_c = 1$. The ordering was reversed at $p_{\text{rep}} = 0.10$: the period fell by 41.5% when $q_c = 0$, compared with 33.7% when $q_c = 1$.

5.3 Neighbourhood size changes the direction of the canalisation effect

The actual Watts–Strogatz neighbourhood parameter κ had a larger effect on adjusted period than network size N. At $\kappa = 1$, increasing N from 10 to 100 changed the adjusted mean log period from 0.203 to 0.338. At $N = 100$, increasing κ from 1 to 5 changed it from 0.338 to 3.450 (Fig. 4A). Predictions in this panel are restricted to simulated N–κ combinations, avoiding extrapolation into combinations absent from the design.

More importantly, κ changed the direction of the canalisation effect (Fig. 4B). At $N = 100$ and $\kappa = 1$, increasing q_c from 0 to 1 increased the adjusted geometric mean period by 22.1%–25.8% across inhibitory-edge probabilities. At $\kappa = 2$, the same contrast reduced the period by 35.3%–45.8%, and reductions generally became larger as κ increased. The main exception was $p_{\text{rep}} = 0.10$, for which the reduction peaked at 55.4% at $\kappa = 3$ and weakened to 20.7% at $\kappa = 5$. At $\kappa = 5$, the reductions for $p_{\text{rep}} = 0.24$–0.50 were 98.8%–99.9%. These contrasts are model predictions for the specified parameter settings at $N = 100$ and should not be interpreted as values expected for every graph.

Neighbourhood size also amplified the effect of inhibitory-edge probability (Fig. 4C). Relative to $p_{\text{rep}} = 0.50$, $p_{\text{rep}} = 0.10$ reduced the adjusted period by 9.6% at $\kappa = 1$, but by 99.3% at $\kappa = 5$. The supplementary pairwise views show that the effects involving N were comparatively small at $\kappa = 1$, the neighbourhood size available for every N (Supplementary Fig. S3A), whereas the κ–p relationship was strongly non-linear at $N = 100$ (Supplementary Fig. S3B). From $p = 0.01$ to $p = 0.60$, adjusted mean log period decreased from 0.422 to 0.294 at $\kappa = 1$, from 2.312 to 1.139 at $\kappa = 2$, and from 2.879 to 1.954 at $\kappa = 3$; it changed little at $\kappa = 4$ (2.795 to 2.771) and increased at $\kappa = 5$ (3.097 to 3.619).

Because the scientific question was whether connectivity changes the joint canalisation–inhibition effect, the $\kappa \times q_c \times p_{\text{rep}}$ interaction was tested explicitly. Adding it reduced design-cell cross-validation RMSE from 0.293 to 0.212 and gave $\Delta\text{AIC} = -2299.95$, so it was retained in the primary model. The corresponding endpoint view at $N = 100$ shows the reversal at $\kappa = 1$ and the distinct $p_{\text{rep}} = 0.10$ pattern at high κ (Supplementary Fig. S4). For example, at $\kappa = 5$, the $q_c = 1$ versus $q_c = 0$ contrast was $\Delta Y = -0.232$ at $p_{\text{rep}} = 0.10$, compared with -4.417 to -6.794 at $p_{\text{rep}} = 0.24$–0.50.

5.4 Canalisation reduces the number of attractors reached from sampled initial states

The fixed-system analysis used $p_{\text{rep}} \in \{0.30, 0.50\}$. Increasing q_c from 0 to 1 reduced the mean number of attractors reached from 200 sampled initial states per system. The mean fell from 12.00 to 4.77 at $p_{\text{rep}} = 0.30$ (difference -7.24, 95% CI $[-9.82, -4.65]$) and from 10.81 to 5.07 at $p_{\text{rep}} = 0.50$ (difference -5.75, 95% CI $[-8.21, -3.28]$; Fig. 5A).

The largest observed basin fraction did not change clearly between $q_c = 0$ and $q_c = 1$. The endpoint difference was 0.024 (95% CI $[-0.007, 0.055]$) at $p_{\text{rep}} = 0.30$ and -0.009 (95% CI $[-0.040, 0.022]$) at $p_{\text{rep}} = 0.50$; both confidence intervals included zero (Fig. 5B). Observed basin entropy decreased from 0.715 to

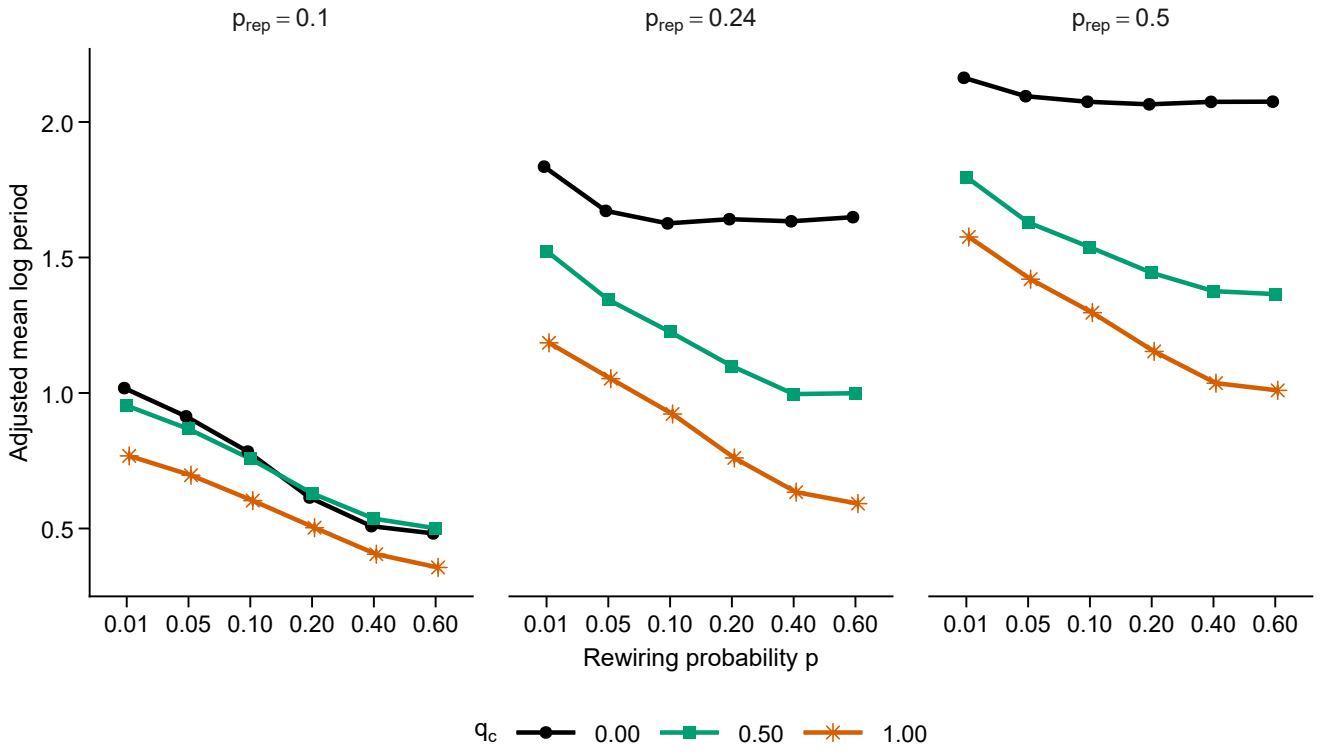


Figure 3: Rewiring modifies the rule effects. Adjusted mean log period is shown across the six controlled rewiring probabilities for $q_c = 0$, 0.50, and 1.00. Panels show the representative inhibitory-edge probabilities $p_{\text{rep}} = 0.10$, 0.24, and 0.50. Predictions are averaged equally over the simulated N–κ combinations. Rewiring probability is plotted as an ordered experimental level so that every label is exact.

0.505 at $p_{\text{rep}} = 0.30$ (difference −0.210, 95% CI $[-0.322, -0.098]$). At $p_{\text{rep}} = 0.50$, the decrease from 0.671 to 0.571 was uncertain because its confidence interval included zero (difference −0.100, 95% CI $[-0.208, 0.008]$; Fig. 5C). Full canalisation therefore reduced the number of attractors reached relative to $q_c = 0$, without a clear increase in the largest observed basin fraction.

The minimum per-system detection rate at $q_c = 0$ was 0.925 for $p_{\text{rep}} = 0.30$ and 0.215 for $p_{\text{rep}} = 0.50$; the minimum was 1.0 in every $q_c > 0$ combination. The threshold-only basin summaries, particularly at $p_{\text{rep}} = 0.50$, should therefore be interpreted as summaries of detected attractors reached from sampled initial states.

5.5 Canalisation improves recovery from one-bit perturbations

The probability of returning to the original attractor within 2000 updates increased with q_c at both inhibitory-edge probabilities (Fig. 6A). From $q_c = 0$ to $q_c = 1$, return probability increased from 0.8905 to 0.9537 at $p_{\text{rep}} = 0.30$ (difference 0.0633, 95% CI $[0.0480, 0.0786]$) and from 0.8817 to 0.9372 at $p_{\text{rep}} = 0.50$ (difference 0.0555, 95% CI $[0.0385, 0.0725]$).

Restricted mean return time, which assigns the 2000-update cap to non-returning trials, also decreased. It fell from 229.9 to 95.2 updates at $p_{\text{rep}} = 0.30$ (difference −134.8, 95% CI $[-166.1, -103.4]$) and from 248.1 to 130.7 updates at $p_{\text{rep}} = 0.50$ (difference −117.4, 95% CI $[-152.2, -82.6]$; Fig. 6B). The Hamming fraction after 25 updates decreased from 0.0337 to 0.0060 and from 0.0386 to 0.0103, respectively; the endpoint differences were −0.0278 (95% CI $[-0.0333, -0.0222]$) and −0.0283 (95% CI $[-0.0345, -0.0220]$; Fig. 6C).

The supplementary perturbation summaries

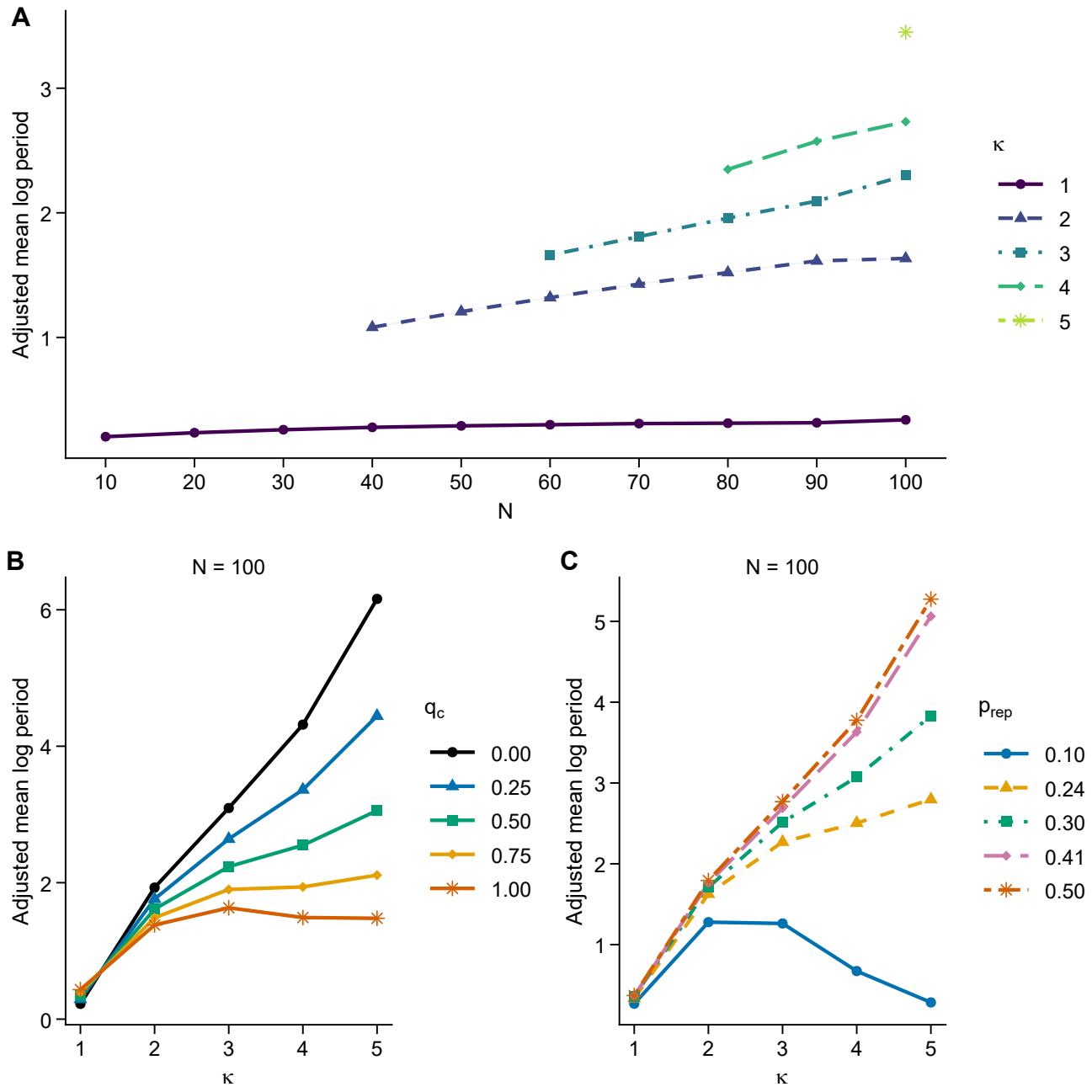


Figure 4: Network size and neighbourhood size modify period dynamics. Panel A shows adjusted mean log period across N and the actual Watts–Strogatz neighbourhood parameter κ, restricted to simulated N–κ combinations. Panels B and C show the interactions of κ with q_c and p_{rep}, respectively, at $N = 100$, where every κ value was simulated.

support the same conclusion (Supplementary Fig. S1). Among successful returns, mean return time decreased from 16.01 to 2.82 updates at $p_{\text{rep}} = 0.30$, and from 18.66 to 5.55 updates at $p_{\text{rep}} = 0.50$. Immediate spread was less consistent: the $t = 1$ Hamming-fraction contrast was supported at $p_{\text{rep}} = 0.30$, but its 95% confidence interval crossed zero at $p_{\text{rep}} = 0.50$. By $t = 10$,

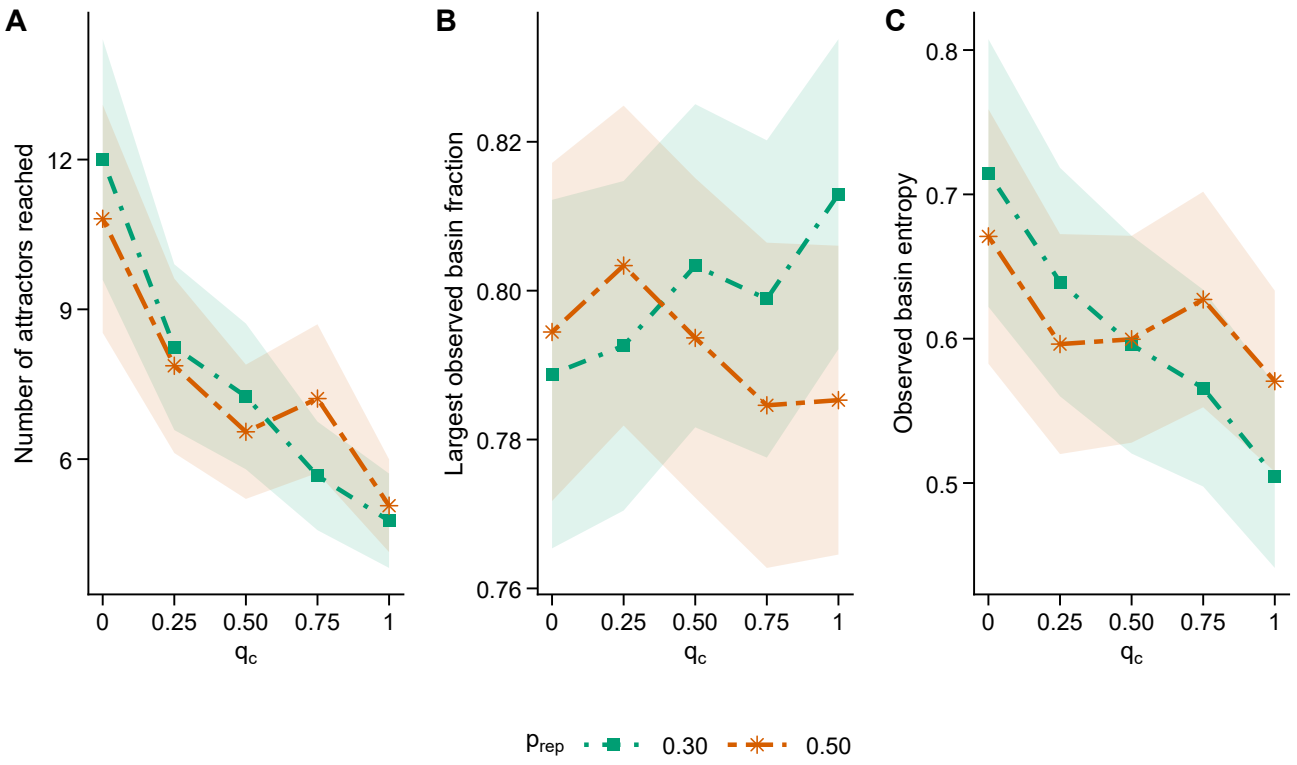


Figure 5: Basin summaries estimated from sampled initial states in the fixed-system design. Panels show (A) the number of attractors reached, (B) the largest observed basin fraction, and (C) observed basin entropy. Each (q_c, p_{rep}) combination contains 720 systems, and each system was evaluated using 200 sampled initial states.

spread was lower under full canalisation at both inhibitory-edge probabilities; the corresponding $t = 25$ result is shown in Fig. 6C.

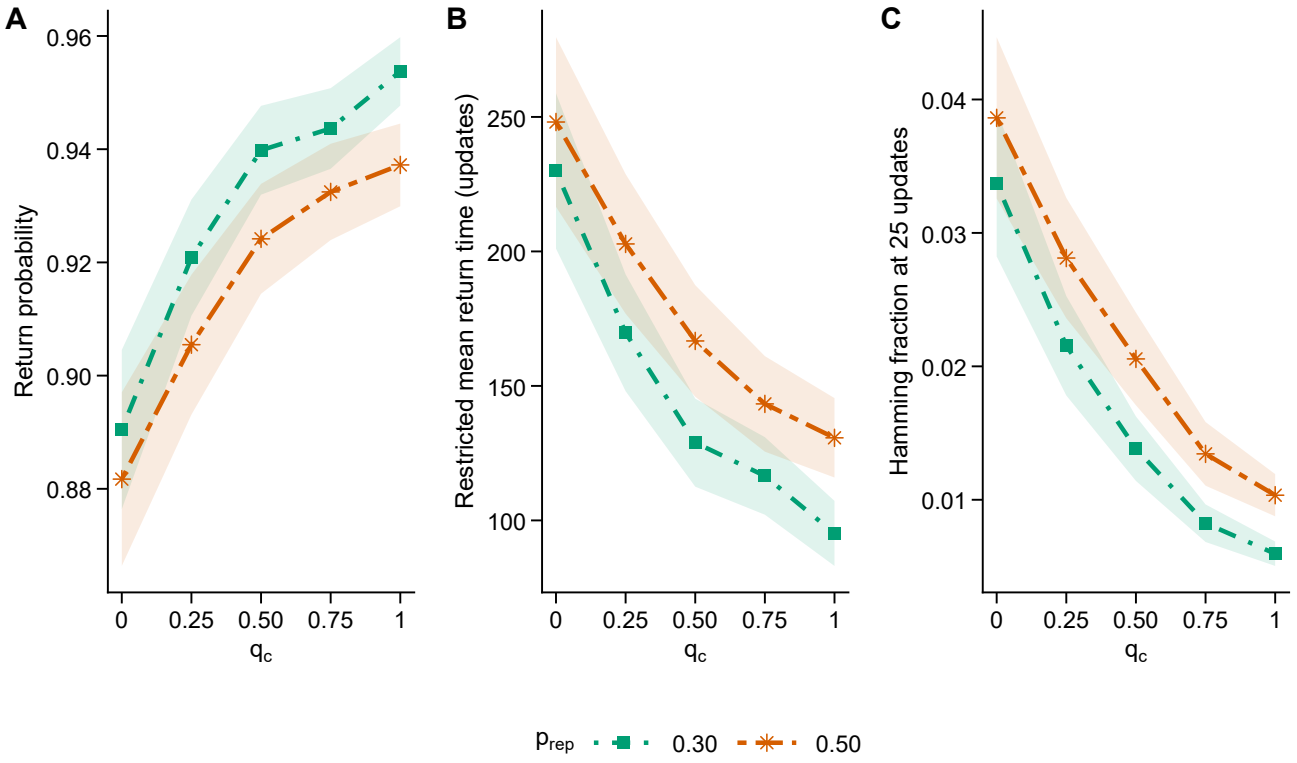


Figure 6: Recovery following a one-bit perturbation in the fixed-system design. Panels show (A) return probability within 2000 updates, (B) restricted mean return time, for which non-returning trials contribute the 2000-update cap, and (C) the Hamming fraction after 25 updates. Each (q_c, p_{rep}) combination contains 720 systems with 30 perturbation trials per system.

6 Discussion

The central result is that the period effect of depth-1 canalisation depends on network context. Canalisation shortened attractor periods across most of the design but reversed direction in the $N = 100$, $\kappa = 1$ comparison, while the response to rewiring varied with the canalisation and inhibitory-edge settings. These results show that network structure and update rules act together [12, 14, 41].

The period reduction under canalisation was not explained by a higher fixed-point rate. The fixed-point rate was lower at $q_c = 1$ than at $q_c = 0$ at every inhibitory-edge probability, including conditions in which attractor periods became substantially shorter (Fig. 2). This distinction is important because shorter periods and more fixed points are different forms of dynamical organisation. The result is consistent with work showing that canalising structure can reduce sensitivity and alter attractor organisation [29, 31, 12, 14].

Inhibitory-edge probability determined how strongly the rule settings affected period. At $p_{\text{rep}} = 0.24$–0.50, the observed and adjusted analyses both showed large period reductions as q_c increased. By contrast, the $p_{\text{rep}} = 0.10$ condition showed only a modest endpoint reduction and a small initial increase at $q_c = 0.25$. Canalisation therefore narrowed, but did not remove, the separation among inhibitory-edge probabilities (Fig. 2C). The effect of a dominant input may therefore depend on the signs of the other inputs and on the fallback threshold rule. When inhibitory-edge probability is low, predominantly activating interactions may leave less long-period behaviour for depth-1 canalisation to suppress.

This is an interpretation of the estimated pattern, not a separately tested causal mechanism.

The neighbourhood parameter κ provided the clearest evidence that canalisation is connectivity-dependent. At $N = 100$ and $\kappa = 1$, full canalisation increased the adjusted geometric mean period across all inhibitory-edge probabilities. From $\kappa = 2$ onward at $N = 100$, it generally shortened the period, with larger reductions at higher connectivity (Fig. 4). Network size N had a smaller effect when compared at $\kappa = 1$, the neighbourhood size available for every N. One possible explanation is that increasing κ gives the fallback threshold rule more inputs and more possible input combinations that may support long-period dynamics. When the canalising value is active, the dominant input overrides the fallback rule and may remove more of this behaviour. At low connectivity, the fallback rule has few inputs, so the same override may change the dynamics rather than shorten them. The $\kappa \times q_c \times p_{\text{rep}}$ interaction and its better grouped predictive performance support this connectivity-dependent pattern, but they do not establish the proposed mechanism. Direct analyses of rule sensitivity and state-transition structure would be needed to test it [11, 12].

Rewiring provided a second interaction between network structure and update rules. After averaging over the simulated structural settings, increasing p from 0.01 to 0.60 shortened adjusted periods in every (q_c, p_{rep}) combination (Fig. 3). However, the connectivity-specific analyses show that this averaged response was not uniform across κ (Supplementary Fig. S3B). This extends the earlier threshold-rule study by showing that the response to Watts–Strogatz rewiring changes when canalisation, inhibitory-edge probability, and connectivity vary [23]. Because p changes several graph properties simultaneously, these contrasts describe the controlled rewiring regime rather than an isolated clustering effect [21, 41].

The fixed-system analyses show that the period results were accompanied by changes in basin summaries and perturbation recovery. Compared with $q_c = 0$, full canalisation reduced the number of attractors reached from sampled initial states at both inhibitory-edge probabilities (Fig. 5). It also reduced observed basin entropy at $p_{\text{rep}} = 0.30$, although the difference was uncertain at $p_{\text{rep}} = 0.50$. The largest observed basin fraction did not change clearly. Canalisation therefore reduced the number of attractors reached without a clear increase in the largest observed basin fraction. A lower number of attractors reached should not be interpreted as evidence that the system has only one attractor [10, 14].

After one-bit perturbations, increasing q_c increased the probability of returning to the original attractor, reduced restricted mean return time, and reduced the Hamming fraction at later observation times (Fig. 6). The immediate response at $t = 1$ was less consistent, whereas the effects at $t = 10$ and $t = 25$ agreed at both inhibitory-edge probabilities. Canalisation did not always prevent the initial spread of a perturbation, but it made that spread less persistent and improved later recovery. Together with the basin results, this indicates better recovery after perturbation and fewer attractors reached from the sampled states. It does not imply universal resistance to perturbation or convergence to fixed points. This interpretation is consistent with the connection between canalising structure, reduced effective sensitivity, and ordered Boolean dynamics [31, 12].

In this model, q_c controls how often nodes with at least one regulator are assigned a canalising rule; it should not be interpreted as a direct molecular measurement. Shoot-branching regulation provides one motivating example because BRANCHED1 (BRC1) integrates several hormonal and environmental signals in axillary buds and can act as a strong local regulator of bud outgrowth [42, 43, 44]. We use this as a biological analogy for dominant-input regulation, not as a claim that the simulated canalising rule represents BRC1 specifically or that one regulator determines the behaviour of an entire biological network.

The conclusions remain conditional on the

model and sampling design. All networks came from a directed, signed Watts–Strogatz construction and were updated synchronously, so the results may not transfer unchanged to scale-free, modular, spatial, or data-derived regulatory networks. The simulated sizes were $N = 10$–100; behaviour in much larger networks was not tested. The canalising construction tested at most one dominant regulator per node, the designated canalising value was fixed, and the fallback logic was a signed-threshold rule. The period analysis targets mean log period and does not describe the full tail of the period distribution. Its trajectories were generated from sampled initial states with threshold perturbations redrawn as specified in the Methods, so they do not provide a complete enumeration of all attractors for one deterministic map. The basin summaries were estimated from 200 sampled initial states per fixed system, and perturbation return was observed over a finite window. The analyses therefore do not establish whether every perturbation would eventually return [9]. The very large high-κ contrasts at $N = 100$ are model predictions for specified parameter settings rather than values expected for every graph.

Future work should test whether the connectivity-dependent reversal observed at $N = 100$ and $\kappa = 1$ persists under alternative network and rule designs. It should examine node sensitivity, effective connectivity, and state-transition structure across κ, as well as larger networks, the full distribution and upper tail of attractor periods, deeper canalising rules, alternative canalising values, and asynchronous or partially synchronous updating. The design should also be repeated in graph families that control clustering, modularity, and degree heterogeneity more independently [45, 46, 47]. Applying the same prespecified period, basin, and perturbation endpoints to literature-supported plant regulatory networks would provide a stronger biological test. For example, these measures could be applied to *Arabidopsis* shoot-branching models. The synthetic results give a specific prediction for such work: conditionally dominant regulation should not alter attractor periods in every network in the same way; the direction and magnitude of its period effect should depend on connectivity and on the balance of activating and inhibitory inputs.

7 Conclusion

Attractor dynamics in directed, signed Watts–Strogatz Boolean networks depended on the combination of network structure and update rules. Canalisation generally shortened attractor periods and improved recovery from perturbation, but it did not shorten periods in every setting. Its period effect depended strongly on inhibitory-edge probability and, at $N = 100$, reversed at $\kappa = 1$. After averaging over the simulated parameter combinations, the comparison from $p = 0.01$ to $p = 0.60$ also showed shorter adjusted periods in every (q_c, p_{rep}) combination, although the rewiring response varied with the rule settings and connectivity. Network size had a smaller effect than neighbourhood size within the simulated settings.

The shorter periods were not explained by a higher fixed-point rate. Compared with $q_c = 0$, full canalisation was associated with fewer attractors reached from sampled initial states, less persistent perturbation spread, and a greater probability of returning to the original attractor within 2000 updates. The main conclusion is therefore conditional: the period effect of dominant-input regulation depends on the network in which it is embedded. Connectivity, the balance of activating and inhibitory edges, rewiring, and canalising rules should be considered together when Boolean models are used to develop hypotheses about regulatory stability.

Acknowledgements

Maram Alqarni is supported by a scholarship from the Saudi Arabian Cultural Mission (SACM). This research was supported by the Australian Research Council through the Australian Research Council Centre of Excellence for Plant Success in Nature and Agriculture (CE200100015).

Author contributions

Maram Alqarni led the study design, literature review, model implementation, simulations, data analysis, fixed-system experiments, figures, tables and manuscript writing. Mark Cooper contributed to the biological framing and interpretation. Diane Donovan contributed to the research direction and provided mathematical and statistical guidance. James Lefevre contributed to the research questions, study design, reduced-threshold formulation and statistical analysis. All authors discussed the results and critically reviewed the manuscript.

Data availability

The code and processed data underlying this article are openly available in Zenodo at https://doi.org/10.5281/zenodo.22785168.

Competing interests

The authors declare no competing interests.

References

[1] S. A. Kauffman. Metabolic stability and epigenesis in randomly constructed genetic nets. *Journal of Theoretical Biology*, 22(3): 437–467, 1969.

[2] Leon Glass and Stuart A Kauffman. The logical analysis of continuous, non-linear biochemical control networks. *Journal of theoretical Biology*, 39(1):103–129, 1973.

[3] Assieh Saadatpour and Réka Albert. Boolean modeling of biological regulatory networks: a methodology tutorial. *Methods*, 62(1):3–12, 2013.

[4] Ahmed Abdelmonem Hemedan, Anna Niarakis, Reinhard Schneider, and Marek Ostaszewski. Boolean modelling as a logic-based dynamic approach in systems medicine. *Computational and Structural Biotechnology Journal*, 20:3161–3172, 2022. doi: 10.1016/j.csbj.2022.06.035.

[5] Carlos Gershenson. Introduction to random boolean networks. *arXiv preprint nlin/0408006*, 2004.

[6] Barbara Drossel. Random boolean networks. *Reviews of nonlinear dynamics and complexity*, pages 69–110, 2008.

[7] Stéphanie Chevalier, Julia Becker, Yujuan Gui, Vincent Noël, Cui Su, Sascha Jung, Laurence Calzone, Andrei Zinovyev, Antonio del Sol, Jun Pang, Lasse Sinkkonen, Thomas Sauter, and Loïc Paulevé. Data-driven inference of boolean networks from transcriptomes to predict cellular differentiation and reprogramming. *npj Systems Biology and Applications*, 11:105, 2025. doi: 10.1038/s41540-025-00569-z.

[8] Martin Hopfensitz, Christoph Müssel, Markus Maucher, and Hans A Kestler. Attractors in boolean networks: a tutorial. *Computational Statistics*, 28:19–36, 2013.

[9] Tomoya Mori and Tatsuya Akutsu. Attractor detection and enumeration algorithms for boolean networks. *Computational and Structural Biotechnology Journal*, 20:2512–2520, 2022. doi: 10.1016/j.csbj.2022.05.027.

[10] Peter Krawitz and Ilya Shmulevich. Basin entropy in boolean network ensembles. *Physical Review Letters*, 98(15):158701, 2007. doi: 10.1103/PhysRevLett.98.158701.

[11] Ilya Shmulevich and Stuart A Kauffman. Activities and sensitivities in boolean network models. *Physical review letters*, 93(4):048701, 2004.

[12] Claus Kadelka, Jack Kuipers, and Reinhard Laubenbacher. The influence of canalization on the robustness of Boolean networks. *Physica D: Nonlinear Phenomena*, 353–354:39–47, 2017. doi: 10.1016/j.physd.2017.05.002.

[13] Elena S. Dimitrova, Oleg I. Yordanov, and Mihaela T. Matache. Difference equation

for tracking perturbations in systems of Boolean nested canalyzing functions. *Physical Review E*, 91(6):062812, 2015. doi: 10.1103/PhysRevE.91.062812.

[14] Elijah Paul, Gleb Pogudin, William Qin, and Reinhard Laubenbacher. The dynamics of canalizing boolean networks. *Complexity*, 2020:3687961, 2020. doi: 10.1155/2020/3687961.

[15] Claus Kadelka and Kishore Hari. Critical assessment of the ability of Boolean threshold models to describe gene regulatory network dynamics. *PNAS Nexus*, 4(8):pgaf228, 2025. doi: 10.1093/pnasnexus/pgaf228.

[16] Van Tran, Matthew N. McCall, Helene R. McMurray, and Anthony Almudevar. On the underlying assumptions of threshold boolean networks as a model for genetic regulatory network behavior. *Frontiers in Genetics*, 4: 263, 2013. doi: 10.3389/fgene.2013.00263.

[17] Winfried Just, Ilya Shmulevich, and John Konvalina. The number and probability of canalizing functions. *Physica D: Nonlinear Phenomena*, 197(3–4):211–221, 2004.

[18] Abdul Salam Jarrah, Blessilda Raposa, and Reinhard Laubenbacher. Nested canalyzing, unate cascade, and polynomial functions. *Physica D: Nonlinear Phenomena*, 233(2): 167–174, 2007. doi: 10.1016/j.physd.2007.06.022.

[19] Daniel McDonald, Laura Waterbury, Rob Knight, and M. D. Betterton. Activating and inhibiting connections in biological network dynamics. *Biology Direct*, 3:49, 2008. doi: 10.1186/1745-6150-3-49.

[20] Ernesto Pérez-Rueda and Julio Collado-Vides. The repertoire of dna-binding transcriptional regulators in Escherichia coli K-12. *Nucleic Acids Research*, 28(8):1838–1847, 2000.

[21] Duncan J Watts and Steven H Strogatz. Collective dynamics of 'small-world' networks. *Nature*, 393(6684):440–442, 1998.

[22] Mark EJ Newman. The structure and function of complex networks. *SIAM review*, 45 (2):167–256, 2003.

[23] Maram Alqarni, Mark Cooper, Diane Donovan, and James Lefevre. Clustering compresses attractors in watts–strogatz threshold boolean networks. *Journal of Complex Networks*, 14(4):cnag027, 2026.

[24] Carl R. Simmons, H. Renee Lafitte, Kellie S. Reimann, Norbert Brugière, Keith Roesler, Marc C. Albertsen, Thomas W. Greene, and Jeffrey E. Habben. Successes and insights of an industry biotech program to enhance maize agronomic traits. *Plant Science*, 307: 110899, 2021. doi: 10.1016/j.plantsci.2021.110899.

[25] Daniel Ortiz-Barrientos, David Jordan, and Mark Cooper. The hidden geometry of breeding constraints. *Nature Plants*, 12:1316–1324, 2026. doi: 10.1038/s41477-026-02332-6.

[26] Owen M. Powell, Lee Hickey, Shunichiro Tomura, and Mark Cooper. Better breeding leveraging more biology. *Trends in Plant Science*, 2026. doi: 10.1016/j.tplants.2026.05.004.

[27] Claus Kadelka, Taras-Michael Butrie, Evan Hilton, Jack Kinseth, Addison Schmidt, and Haris Serdarevic. A meta-analysis of boolean network models reveals design principles of gene regulatory networks. *Science Advances*, 10(2):eadj0822, 2024. doi: 10.1126/sciadv.adj0822.

[28] Lingyu Li, Liangjie Sun, Guangyi Chen, Chi-Wing Wong, Wai-Ki Ching, and Zhi-Ping Liu. LogBTF: gene regulatory network inference using boolean threshold network model from single-cell gene expression

data. *Bioinformatics*, 39:btad256, 2023. doi: 10.1093/bioinformatics/btad256.

[29] Stuart Kauffman, Carsten Peterson, Björn Samuelsson, and Carl Troein. Genetic networks with canalyzing boolean rules are always stable. *Proceedings of the National Academy of Sciences*, 101(49):17102–17107, 2004. doi: 10.1073/pnas.0407783101.

[30] Yuan Li, John O. Adeyeye, David Murrugarra, Boris Aguilar, and Reinhard Laubenbacher. Boolean nested canalizing functions: A comprehensive analysis. *Theoretical Computer Science*, 481:24–36, 2013. doi: 10.1016/j.tcs.2013.02.020.

[31] Lori Layne, Elena Dimitrova, and Matthew Macauley. Nested canalyzing depth and network stability. *Bulletin of Mathematical Biology*, 74(2):422–433, 2012. doi: 10.1007/s11538-011-9692-y.

[32] Alexander J. Gates, Rion Brattig Correia, Xuan Wang, and Luis M. Rocha. The effective graph reveals redundancy, canalization, and control pathways in biochemical regulation and signaling. *Proceedings of the National Academy of Sciences*, 118:e2022598118, 2021. doi: 10.1073/pnas.2022598118.

[33] Claus Kadelka and David Murrugarra. Canalization reduces the nonlinearity of regulation in biological networks. *npj Systems Biology and Applications*, 10(1):67, 2024. doi: 10.1038/s41540-024-00392-y.

[34] Reinhard Diestel. *Graph Theory*. Springer, 5th edition, 2017.

[35] Frank Harary. *Graph Theory*. Addison-Wesley, 1969.

[36] M. E. J. Newman. Mathematics of networks. In Steven N. Durlauf and Lawrence E. Blume, editors, *The New Palgrave Dictionary of Economics*, pages 4059–4064. Palgrave Macmillan, London, 2nd edition, 2008. doi: 10.1007/978-1-349-58802-2_1061.

[37] Réka Albert and Albert-László Barabási. Statistical mechanics of complex networks. *Reviews of Modern Physics*, 74(1):47–97, 2002. doi: 10.1103/RevModPhys.74.47.

[38] Assieh Saadatpour, István Albert, and Réka Albert. Attractor analysis of asynchronous Boolean models of signal transduction networks. *Journal of Theoretical Biology*, 266 (4):641–656, 2010. doi: 10.1016/j.jtbi.2010.07.022.

[39] Maximino Aldana and Philippe Cluzel. A natural class of robust networks. *Proceedings of the National Academy of Sciences*, 100 (15):8710–8714, 2003.

[40] Gareth James, Daniela Witten, Trevor Hastie, and Robert Tibshirani. *An introduction to statistical learning: with applications in R*, volume 103. Springer, 2013.

[41] Andrew Pomerance, Edward Ott, Michelle Girvan, and Wolfgang Losert. The effect of network topology on the stability of discrete state models of genetic control. *Proceedings of the National Academy of Sciences*, 106 (20):8209–8214, 2009.

[42] Min Wang, Marie-Angélique Le Moigne, Jessica Bertheloot, Laurent Crespel, María-Dolores Pérez-Garcia, Lucie Ogé, Sylvie Demotes-Mainard, Latifa Hamama, Jean-Michel Davière, and Soulaiman Sakr. BRANCHED1: A key hub of shoot branching. *Frontiers in Plant Science*, 10:76, 2019. doi: 10.3389/fpls.2019.00076.

[43] Catherine Rameau, Jessica Bertheloot, Nathalie Leduc, Bruno Andrieu, Fabrice Foucher, and Soulaiman Sakr. Multiple

pathways regulate shoot branching. *Frontiers in Plant Science*, 5:741, 2015. doi: 10.3389/fpls.2014.00741.

[44] François F. Barbier, Elizabeth A. Dun, Stephanie C. Kerr, Tinashe G. Chabikwa, and Christine A. Beveridge. An update on the signals controlling shoot branching. *Trends in Plant Science*, 24(3):220–236, 2019. doi: 10.1016/j.tplants.2018.12.001.

[45] Mark EJ Newman. Random graphs with clustering. *Physical review letters*, 103(5): 058701, 2009.

[46] Joel C Miller. Percolation and epidemics in random clustered networks. *Physical Review E—Statistical, Nonlinear, and Soft Matter Physics*, 80(2):020901, 2009.

[47] Shweta Bansal, Shashank Khandelwal, and Lauren Ancel Meyers. Exploring biological network structure with clustered random networks. *BMC Bioinformatics*, 10:405, 2009. doi: 10.1186/1471-2105-10-405.

Supplementary Files

This is a list of supplementary files associated with this preprint. Click to download.

- SupplementaryInformation.pdf